applied sciences

MDPI

Article

Analysis of Dust Detection Algorithms Based on FY-4A Satellite Data

Lu Yang [1], Lu She [1,*], Yahui Che [2,*], Xingwei He [3], Chen Yang [1] and Zixian Feng [1]

[1] School of Geography and Planning, Ningxia University, Yinchuan 750021, China
[2] School of Engineering and Built Environment, Griffith University, Kessels Road, Brisbane, QLD 4111, Australia
[3] Key Laboratory of Radiometric Calibration and Validation for Environmental Satellites, National Satellite Meteorological Center (National Center for Space Weather), China Meteorological Administration, Beijing 100081, China
* Correspondence: shelu_whu@nxu.edu.cn (L.S.); yahui.che@griffithuni.edu.au (Y.C.)

Abstract: Dust detection is essential for environmental protection, climate change assessment, and human health issues. Based on the Fengyun-4A (FY-4A)/Advance Geostationary Radiation Imager (AGRI) images, this paper aimed to examine the performances of two classic dust detection algorithms (i.e., the brightness temperature difference (BTD) and normalized difference dust index (NDDI) thresholding algorithms) as well as two dust products (i.e., the infrared differential dust index (IDDI) and Dust Score products (DST) developed by the China Meteorological Administration). Results show that a threshold below −0.4 for BTD (11–12 µm) is appropriate for dust identification over China and that there is no fixed threshold for NDDI due to its limitations in distinguishing dust from bare ground. The IDDI and DST products presented similar results, where they are capable of detecting dust over all study areas only for daytime. A validation of these four dust detection algorithms has also been conducted with ground-based particulate matter (PM10) concentration measurements for the spring (March to May) of 2021. Results show that the average probability of correct detection (POCD) for BTD, NDDI, IDDI, and DST were 56.15%, 39.39%, 48.22%, and 46.75%, respectively. Overall, BTD performed the best on dust detection over China with its relative higher accuracy followed by IDDI and DST in the spring of 2021. A single threshold for NDDI led to a lower accuracy than those for others. Additionally, we integrated the BTD and IDDI algorithms for verification. The POFD after integration was only 56.17%, and the fusion algorithm had certain advantages over the single algorithm verification.

Keywords: dust detection; FY-4A; BTD; NDDI; IDDI; DST

check for updates

Citation: Yang, L.; She, L.; Che, Y.; He, X.; Yang, C.; Feng, Z. Analysis of Dust Detection Algorithms Based on FY-4A Satellite Data. *Appl. Sci.* **2023**, *13*, 1365. https://doi.org/10.3390/app13031365

Academic Editor: Harry D. Kambezidis

Received: 13 December 2022
Revised: 13 January 2023
Accepted: 17 January 2023
Published: 19 January 2023

Copyright: © 2023 by the authors. Licensee MDPI, Basel, Switzerland. This article is an open access article distributed under the terms and conditions of the Creative Commons Attribution (CC BY) license (https://creativecommons.org/licenses/by/4.0/).

1. Introduction

Dust storm is a natural disaster that causes enormous damage to the environment, transportation, and crops [1]. It also has direct and indirect impacts on public health and human health [2,3]. Small volumes of dust particles can enter the respiratory tract and lungs, causing asthma, pneumonia, and other respiratory and cardiovascular diseases [4,5]. Studies have shown that exposure to dust particles in the air for hours to days can lead to other problems such as conjunctivitis, meningitis, and valley fever [6–9]. There are currently four major dust source areas and dust-prone zones in the world, located in northern Africa, eastern Asia, North America, and Australia [10]. The Taklamakan and Gobi Deserts in northwestern China are the main dust source in East Asia and also the second largest dust source in the world [10]. Dust storm episodes typically occur in the spring (March–May) [11,12] and cause great damage to the economy and people's lives. Therefore, there are economic, social, and scientific benefits from monitoring dust storms and understanding the transport, spatial, and temporal distribution of dust [13,14].

Dust monitoring can be achieved by ground-based observations and satellite remote sensing [15,16]. Data from ground-based air quality monitoring stations are often used to study dust events [17]. However, due to the limited number of ground stations, the dynamic monitoring of dust transport is challenging based on ground-based observations. Dust mainly occurs in desert areas where meteorological stations are not easy to set up and maintain [18]. With the development of meteorological satellite technology, remote sensing images with a high observation frequency and wide spatial coverage play an essential role in dust detection and monitoring [19]. Satellite remote sensing can not only determine the dust source, transport path, impact range, and intensity of dust events but also monitor the dynamics of dust formation, development, and spread [20].

Theoretically, airborne dust can be detected with different optical properties in the ultraviolet (UV), visible (VIS), and infrared (IR) satellite images [21]. Dust detection methods can be generally divided into three categories depending on the channels used. The first category is based on the absorbability of dust aerosols at shorter wavelengths [22]. Typical examples are the absorbing aerosol index from Ozone Monitoring Instrument (OMI) [22,23] and the normalized difference dust index (NDDI) proposed by Qu et al. [24]. Second, methods based on the brightness temperature (BT) in thermal infrared (TIR) channels are more widely used due to the capability to detect dust over bright surfaces and at night [25,26]. Among them, the brightness temperature difference (BTD) between two IR channels [27,28] and infrared difference dust index (IDDI) [29] are the two classic dust detection methods. According to Ackerman [27], the BTD between 8.5, 11, and 12 μm of Moderate Resolution Imaging Spectroradiometer (MODIS) data is capable of detecting dust aerosols. Negative BTD between 11 μm and 12 μm (BTD (11–12 μm)) typically indicate dust presence. IDDI is more often applied to geostationary satellites and has also been used in the operational dust monitoring system in China [30]. Based on the above two types of methods, the combination of shortwave reflectance and infrared brightness temperatures to detect dust have also been developed [31–33]. Table 1 lists several representative indices for dust detection based on the reflectivity and emissivity of airborne dust at multiple channels. However, the ability of these methods are influenced by various factors such as sensor spectral channel configurations and the target area's surface reflection and thermal characteristics. In recent years, machine learning has been increasingly used to detect dust with satellite data [34–36]. Due to the powerful learning capability of machine learning, it has shown high accuracy in regional dust monitoring. The machine learning approach, however, has some drawbacks for detecting dust such as difficulty for large area and near-real-time applications due to the computation requirements and easy over-fitting, especially in the presence of redundant features [37].

Table 1. Summary of the dust detection algorithms.

Channel Type	Dust Index	Algorithm	Reference
VIS and NIR	NDDI	$(R_{0.469} - R_{2.13})/(R_{0.469} - R_{2.13})$	Qu et al. (2006) [24]
	Dust aerosol index (DAI)	$DAI = -100[\log_{10}(R_{412nm}/R_{440nm}) - \log_{10}(R'_{412nm}/R'_{440nm})]$ Nondust absorbing aerosol index (NDAI) $= -10[\log_{10}(R_{412nm}/R_{2130nm})]$	Ciren et al. (2014) [38]
TIR	BTD	BTD (11–12 μm)	Ackerman (1997) [28]
		BTD (3.7–11 μm)	Ackerman (1989) [27]
		BTD (8.5–11 μm)	Ackerman (1997) [28]
	IDDI	$BT_i - BT_j$, where i represents the real-time target brightness temperature, j represents the background brightness temperature	Legrand et al. (2001) [29]
	Thermal infrared dust index (TDI)	$C_0 + C_1 \times BT_{3.7} + C_2 \times BT_{9.7} + C_3 \times BT_{11} + C_4 \times BT_{12}$	Hao and Qu (2007) [39]
	Middle East dust index (MEDI)	$(BT_{11} - BT_{8.5})/(BT_{12} - BT_{8.5})$	Karimi et al. (2012) [40]
	Brightness temperature adjusted difference index (BADI)	$2/\Pi \times \arctan(BDI/BDI_{0.95})$, Where $BDI = (BT_{3.9} - BT_{11.2})^2 \times (BT_{12.4} - BT_{11.2})$	Yue et al. (2017) [41]
VIS, NIR, and TIR	D-parameter	$\mathrm{Exp}(-(R_{0.54}/R_{0.86} + (BT_{11} - BT_{12}) - b)$	Roskovensky and Liou (2005) [42]

Compared to polar-orbiting satellites, the geostationary satellites have a higher frequency of observations, making them more suitable for dust detection [16,43]. Geostationary satellites used to study dust monitoring for China include the Multifunctional Transport Satellite (MTSAT-2) and Himawari 8 launched by Japan [12] and Feng Yun-2 (FY-2) [30] and Feng Yun-4 (FY-4) [44] launched by China. Himawari-8 and FY-4A, as the new generation of geostationary satellites, are superior to MTSAT-2 and FY-2 in terms of temporal resolution, spatial resolution, and the number of measurement channels. Compared to Himawari-8, FY-4A is more appropriate for dust storm monitoring over China, with a broad observation range covering the entirety of China. Jiang et al. [44] conducted FY-4A-based dust monitoring based on machine learning and found that machine learning has the advantage in identifying dust over specific areas. Gao et al. [45] analyzed three dust events that occurred in 2021 with FY-4A data. Additionally, the China Meteorological Administration (CMA) developed two dust products based on FY-4A data including the dust score product (DST) and dust intensity product (IDDI_BK). Wu et al. [46] found that these two FY-4A L2 dust detection products in the northwest region agreed well with the MODIS AOD products. All of these studies demonstrate that FY-4A has good potential for dust detection.

So far, few studies have comprehensively and quantitatively evaluated the performance of different dust detection methods based on FY-4A for dust detection over China. Therefore, this study aimed to evaluate the ability of the BTD, NDDI, CMA IDDI, and DST algorithms/products to detect dust. Focusing on dust detection over China based on FY-4A data, this study:

(1) Qualitatively evaluated the performance of the four algorithms/products on the dust identification during two typical dust events;
(2) Quantitatively compared the BTD, NDDI, and two FY-4A dust products with the real-time ground-based PM10 (less than 10μm in aerodynamic diameter) concentration data and assess their accuracy in identifying dust in the spring of 2021.

2. Study Area and Data

2.1. Study Area

Figure 1 shows the study area. The background shows the land cover types from the GlobeLand30 datasets (http://www.globallandcover.com/ (accessed on 15 January 2022)) [47,48]. The main dust source areas (i.e., the Taklamakan Desert and Gobi Desert) are located in northwestern and North China, respectively, which are dominated by bare land and shrubland. The Taklamakan Desert, located in the middle of the Tarim Basin in southern Xinjiang is the largest desert in China and the second largest mobile desert in the world. The Gobi Desert is located between China and Mongolia, bordered by the Taklamakan Desert to the west and surrounded by the Altai Mountains, the Mongolian steppe, the Hexi Corridor, and the Qinghai–Tibet Plateau, covering parts of northern and northwestern China and the southern part of Mongolia. The dust storms originated from the Taklamakan and Gobi Deserts not only caused severe dust problems in the northwest and north [33,49], but also influenced regions far from dust sources in central China and eastern China due to the long-distance transport of dust plumes [50]. Most dust storms occur during spring due to the climatic and land surface conditions.

2.2. Dataset

2.2.1. FY-4A Data

FY-4A, the China's new generation geostationary orbit meteorological satellite, was launched on 11 December 2016. The Advance Geostationary Radiation Imager (AGRI) is one of the primary payloads on FY-4A and has 14 channels including two VIS, four NIR, and eight IR channels (Table 2). The AGRI imager acquires 40 full-disk maps and 165 regional maps of China on a daily basis, with a regional observation range of 3–55° N and 60–137° E. The FY-4A/AGRI data are publicly available from the National Satellite Meteorological Center data service network (http://satellite.nsmc.org.cn/PortalSite/Default.aspx

(accessed on 10 November 2021)). In this study, FY-4A/AGRI L1 (level 1) data with a 4 km resolution was used.

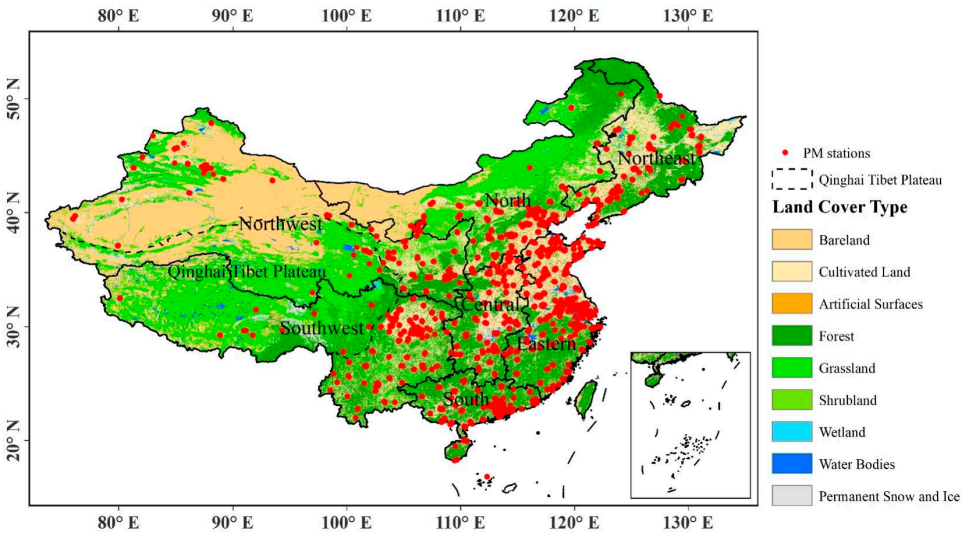

Figure 1. Study area land cover type and PM stations.

Table 2. The main technical parameters of FY-4A AGRI.

Waveband	Spectral Properties	Central Wavelength	Spatial Resolution/km
NOMChannel01	VIS	0.47	1
NOMChannel02		0.65	0.5
NOMChannel03	NIR	0.825	1
NOMChannel04		1.375	2
NOMChannel05		1.61	2
NOMChannel06		2.225	2–4
NOMChannel07	IR	3.75	2–4
NOMChannel08		3.75	4
NOMChannel09		6.25	4
NOMChannel10		7.1	4
NOMChannel11		8.5	4
NOMChannel12		10.8	4
NOMChannel13		12	4
NOMChannel14		13.5	4

2.2.2. FY-4A DSD Data

FY-4A DSD is a dust detection dataset based on the FY-4A AGRI data, which has a spatial resolution of 4 km and a temporal resolution of 1 h and is available on the National Satellite Meteorological Center's Data Services Network (http://satellite.nsmc.org.cn/PortalSite/Default.aspx (accessed on 8 March 2022)). DSD is based on the spectral threshold method and the probability density function (PDF) to distinguish dust and soot from clouds, clear air, and water bodies on land. It uses the individual variability of dust in each spectral display from clouds, the surface, and clear atmosphere [51]. The DST and IDDI products from the DSD dataset were used in this study. DST is determined by the number of the passed dust detection indicators and the PDF function of their thresholds. The higher the score, the greater the possibility of dust. The recommended dust fraction is over 16 for dust pixels, 14–16 for possible dust pixels, and below 14 for non-dust pixels [51]. IDDI is based on the idea that dust causes attenuation of the infrared signal emitted from the surface, resulting in a reduction in the brightness temperature detected by the satellite [29]. IDDI depicts the difference between the sensor observed BT (brightness temperature) and BT from the clear-sky image, which allows for a semi-quantitative description of dust

intensity [51]. It can take full advantage of high-frequency observations from geostationary satellites to dynamically monitor dust movement and intensity evolution.

2.2.3. Particulate Matter (PM) Data

PM10 concentration data (Figure 1) were quality controlled according to the Ambient Air Quality Standard (GB3095-2012) [52] and is available on the national real-time urban air quality release platform of the National Environmental Monitoring Station of China (http://www.cnemc.cn/ (accessed on 16 April 2022)). Hourly PM10 concentration data from March to May 2021 were used in this study to show the validity of the dust detection methods.

3. Methods

The following section describes the dust detection methods applied in this study and the evaluation metrics of the dust detection methods.

3.1. Brightness Temperature Difference (BTD)

BTD (11–12 μm) was first developed primarily for the detection of volcanic aerosols and used for dust detection due to the similarity between mineral dust aerosols and volcanic aerosols [53]. The basic principle is that in the TIR bands, the difference in the imaginary part of dust aerosol refraction affects the atmospheric radiation of dust weather, resulting in BT12 μm greater than 11 μm [54]. Negative BTD (11–12 μm) values typically indicate the presence of dust [27].

The central wavelengths of the NOMChannel12 and NOMChannel13 from FY-4A are 10.8 μm and 12 μm, respectively. In this study, the BTD was calculated as follows:

$$BTD = BT_{NOMChannel12} - BT_{NOMChannel13} \quad (1)$$

Studies have revealed that the BTD thresholds for dust vary depending on the sensors used and the location. Darmenov and Sokolik found BTD thresholds of −1.0, −0.4, 0.5, and −0.2 for the Gobi/Taklamakan, Australian, Nubian, and Thar Deserts, respectively [26], indicating that there is not a universally applicable threshold. In this study, the dust identification threshold of BTD was set to less than −0.4. In order to determine an appropriate threshold to distinguish dust pixels from other pixels in this area, the true color image was classified into dust, cloud, and bare ground pixels with visual interpretation. Figure 2a shows the frequency distribution of the BTD (11–12 μm) values. A total of 51.1% of the BTD values were located around the peak from −1.8 to −3.3. There was only a very small portion of dust pixels with BTD exceeding −0.4. Thus, a BTD value less than −0.4 was identified as dust.

3.2. Normalized Difference Dust Index (NDDI)

Using the VIS and NIR bands, dust storms over low-reflectivity surfaces can be well monitored. Qu et al. [24] proposed the NDDI using MODIS reflectance and found that dust had the lowest reflectance in the 0.469 μm band and the highest reflectance in the 2.13 μm band. This is opposite to clouds. This difference allows for a good distinction of dust from the water/ice clouds and ground features. NDDI has been successfully applied to dust detection in Asia and Africa [55]. For the FY-4A/AGRI data, the NDDI can be calculated as follows:

$$NDDI = (R_{NOMChannel06} - R_{NOMChannel01})/(R_{NOMChannel06} + R_{NOMChannel01}) \quad (2)$$

where $R_{NOMChannel06}$ and $R_{NOMChannel01}$ denote the top of atmosphere reflectance at NOMChannel06 and NOMChannel01. Depending on the area, different NDDI thresholds are used for dust monitoring [56,57].

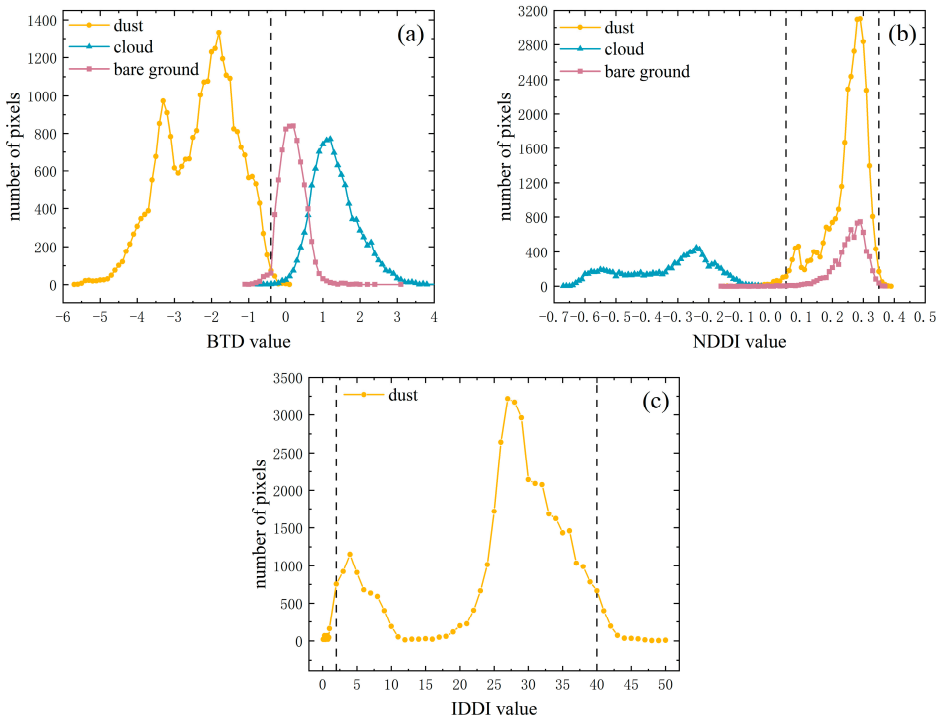

Figure 2. Frequency distribution of the BTD (**a**), NDDI (**b**), and IDDI (**c**) values for dust events.

For dusty pixels, the NDDI threshold was set to 0.05–0.35 in this study. Figure 2b shows the frequency distribution map of NDDI values for the selected dust, cloud, and bare ground pixels. Clouds can be effectively screened using negative NDDI values. However, the NDDI values were higher for both dust and bare ground, so it is difficult to distinguish dust from bare ground.

3.3. Infrared Difference Dust Index (IDDI)

As Figure 2c shows, the frequency distribution of FY-4A IDDI had two peaks for the dusty pixels. In order to not miss the dusty pixels or misclassification, thresholds of 2–40 were set for dust, where the dust pixels began to rise and fall obviously, as the threshold values of IDDI.

3.4. Infrared Difference Dust Index (DST)

As Section 2.2.2 described, the higher the DST, the greater the possibility of dust. The thresholds for DST was set to 16 and pixels greater than 16 were considered to be dust.

3.5. Performance Indicators (POCD and POFD)

The accuracy of the dust areas identified by satellite needs to be validated by ground-based data [15]. The AERONET site AOD measurements and the Ångström exponent have been commonly used to verify the accuracy of dust detection algorithms [58]. There are, however, few AERONET sites located in northwestern China, providing valid observations. PM10 concentration data are an alternative for validation. This is because (1) the PM10 concentration is sensitive to the change in large particles in the near ground atmosphere, especially dust particles, and (2) the high temporal frequency of PM10 concentration observations facilitates the validation of the high temporal resolution geostationary satellite identification results. According to the Ecology and Environment Department's Technical Provisions on Dust Weather Classification, a PM10 concentration greater than 600 $\mu g \cdot m^{-3}$ per hour is considered as dust weather [59]. Thus, any National Environmental Monitoring Station measurement with a PM10 concentration greater than 600 $\mu g \cdot m^{-3}$ was classified as a dusty observation.

The probability of the correct detection (POCD) and the probability of false detection (POFD) were selected to indicate the accuracy of the dust detection results [33,38]:

$$\text{POCD (\%)} = (\text{YY})/(\text{YY} + \text{YN}) \quad (3)$$

$$\text{POFD (\%)} = (\text{NY})/(\text{YY} + \text{NY}) \quad (4)$$

where YY represents the number of matched points where the PM10 concentration is greater than 600 $\mu g \cdot m^{-3}$ and the AGRI dust detection result indicates 'dust', YN represents the number of matched points where the PM10 concentration is greater than 600 $\mu g \cdot m^{-3}$, while the AGRI detection result indicates 'no dust'. NY represents the number of matched points where PM10 is below 600 $\mu g \cdot m^{-3}$, while the AGRI detection result indicates 'dust'.

4. Results and Validation

These four algorithms/products were qualitatively compared with the color composite images during two typical dust events. The two case studies on 15 May 2019 and 16 March 2021 were chosen to demonstrate how the four dust detection methods performed in the two different types of events over China. The first dust event occurred mainly in northwest China, while another dust event affected a wider area, mainly originating in the Gobi Desert and affecting northern China. The BTD and NDDI algorithms were also applied to three months of FY4A/AGRI data. The dust detection results from four algorithms/products were quantitatively compared with the dust identification results from the PM10 concentration measurements in the spring of 2021.

4.1. Analysis of Typical Dust Events

Figure 3a,g,m,s shows the AGRI true color images and dust detection at a 2 h interval between 02:00 and 08:00 UTC on 15 May 2019. In Figure 3, true color images show a dust storm occurring in northwest China including eastern Xinjiang, the Hexi Corridor, and in central Inner Mongolia in North China. The PM10 concentrations increased significantly in northwest, north, and northeast China (Figure 3b,h,n,t).

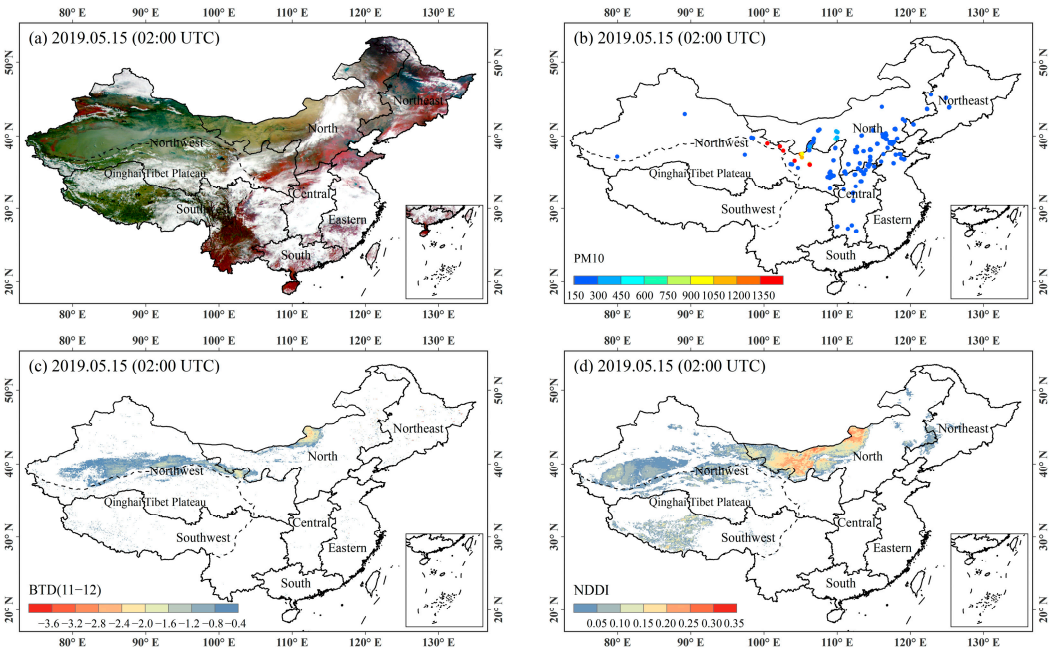

Figure 3. *Cont.*

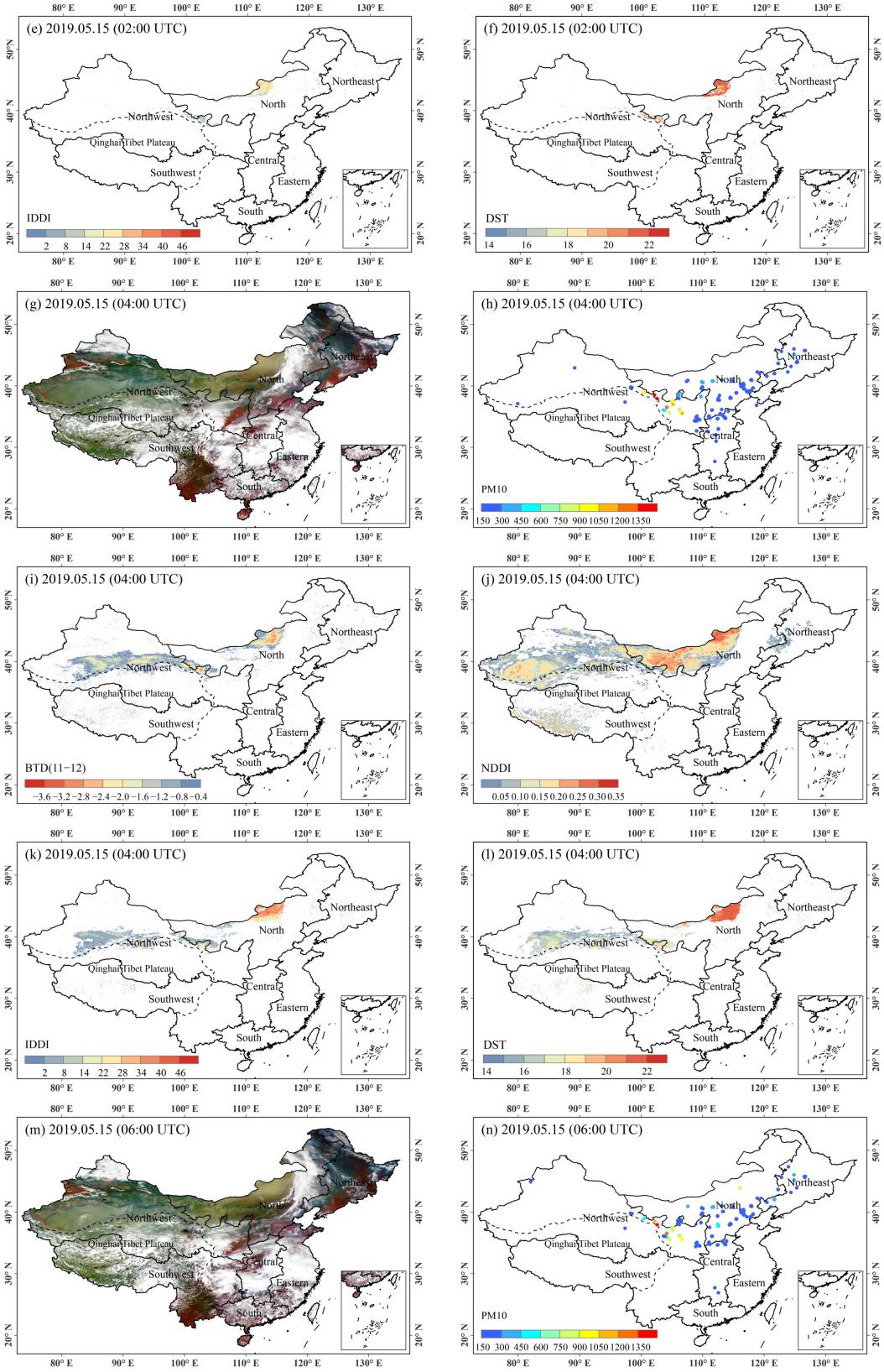

Figure 3. *Cont.*

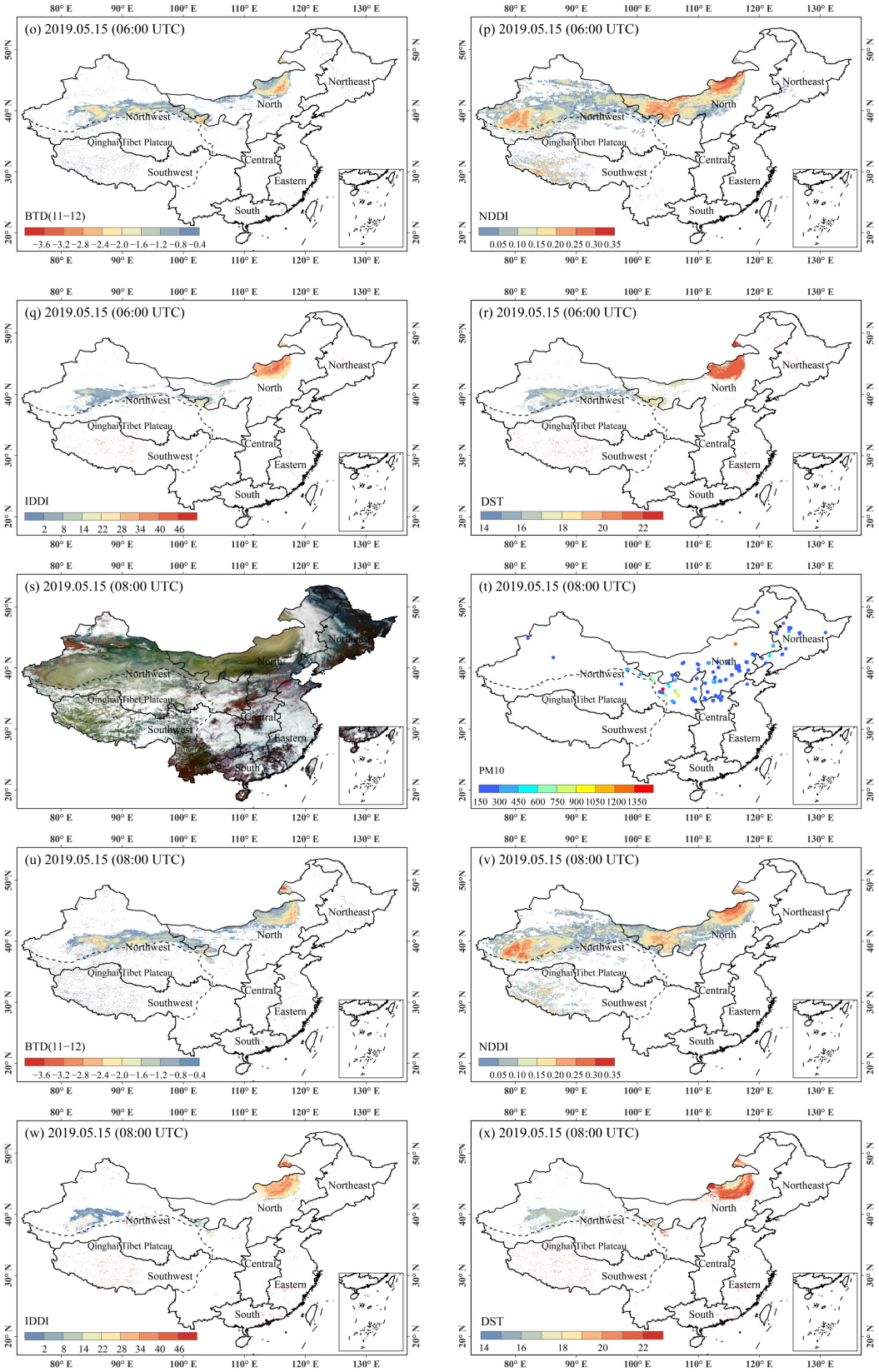

Figure 3. FY-4A AGRI true color images (**a**,**g**,**m**,**s**), PM10 (**b**,**h**,**n**,**t**), BTD (**c**,**i**,**o**,**u**), NDDI (**d**,**j**,**p**,**v**), IDDI (**e**,**k**,**q**,**w**), and DST (**f**,**l**,**r**,**x**) corresponding to the times of 15 May 2019 from 02:00 to 08:00 UTC, respectively.

IDDI and DST from 04:00 to 08:00 UTC showed very similar dust spatial distribution in the FY-4A AGRI true color images and were very similar to the BTD detections. However, there were limitations in detecting dust in parts of the northwest at 02:00 UTC because IDDI and DST are not available when the area is in darkness [46]. The figures show that dust is much more severe in northern China than in northwest China (Figure 3e,k,q,w). Compared to BTD, the DST detection results (over 16) coincided more with the spatial distribution of IDDI.

Figure 4 shows the AGRI true color images and dust detection results at a 2 h interval from 02:00 to 08:00 UTC on 16 March 2021. The dust affected a wider area originating in the Gobi Desert and affecting northern China and even eastern and central China (Figure 4a,g,m,s). The PM10 concentration even exceeded 1320 μg·m^{-3} over the eastern part of northwest China during this dusty weather process, and PM10 concentrations over 450 μg·m^{-3} were observed in central and eastern China. The PM10 concentration dispersion aligned well with the dusty weather process (Figure 4b,h,n,t).

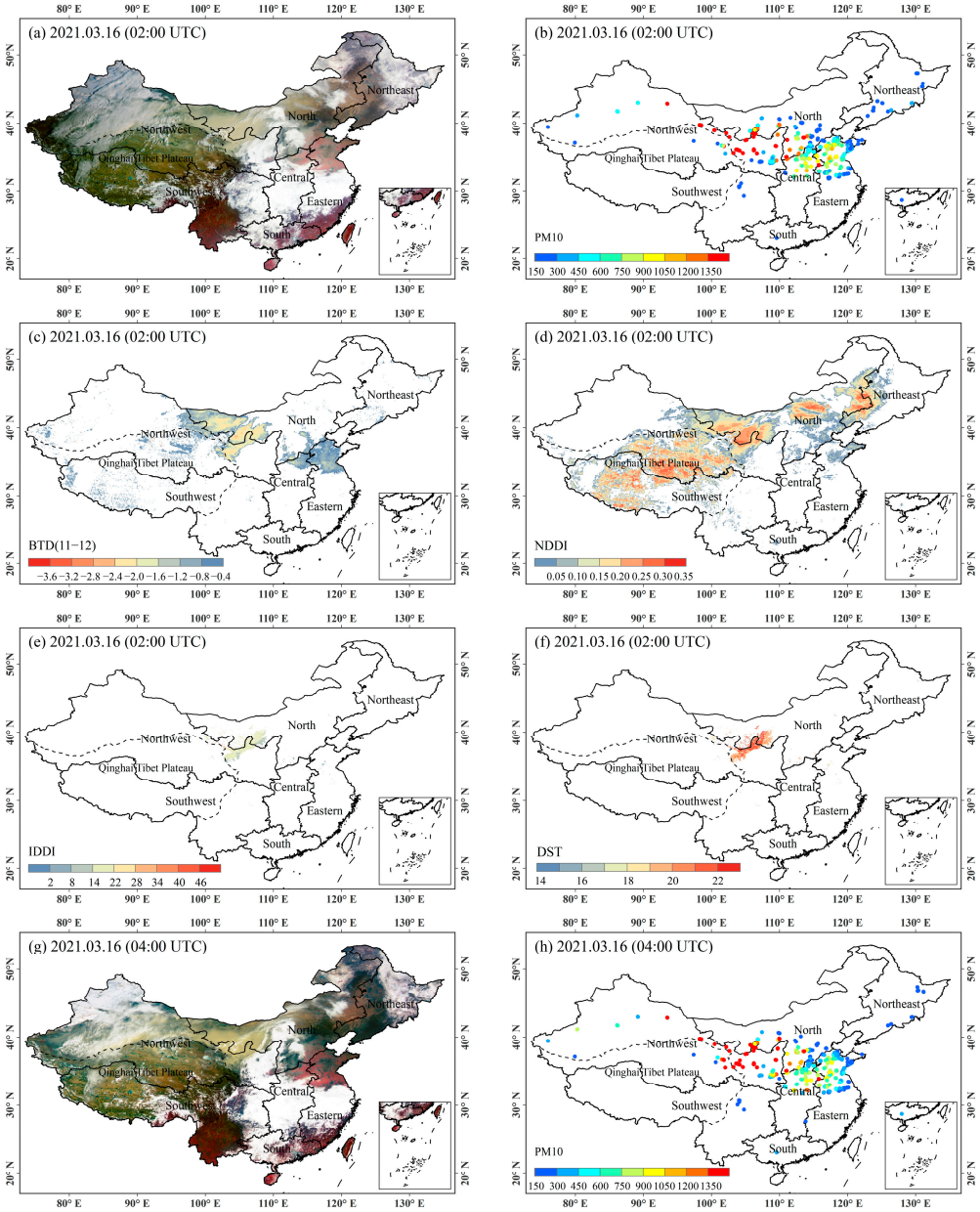

Figure 4. *Cont.*

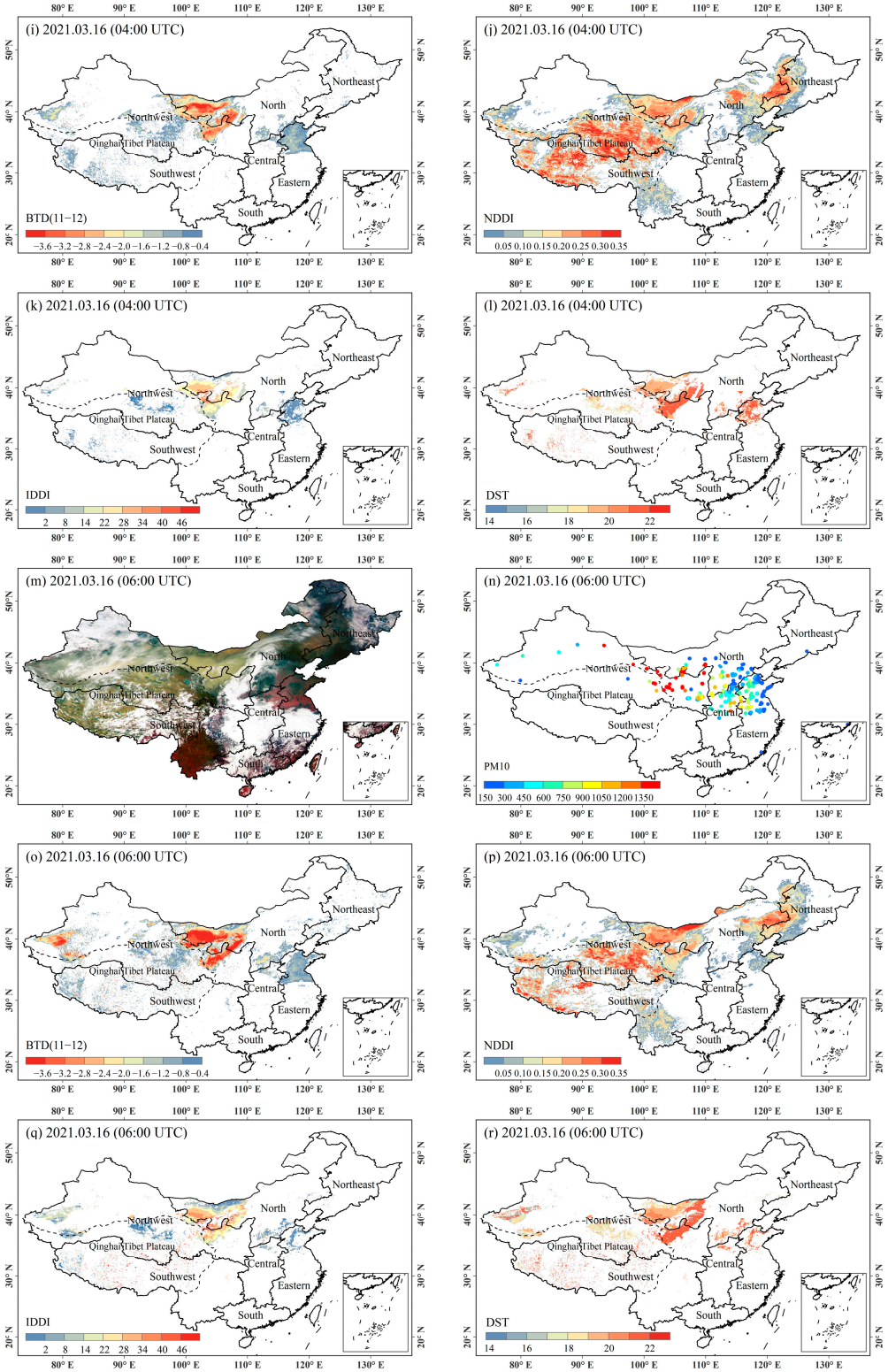

Figure 4. *Cont.*

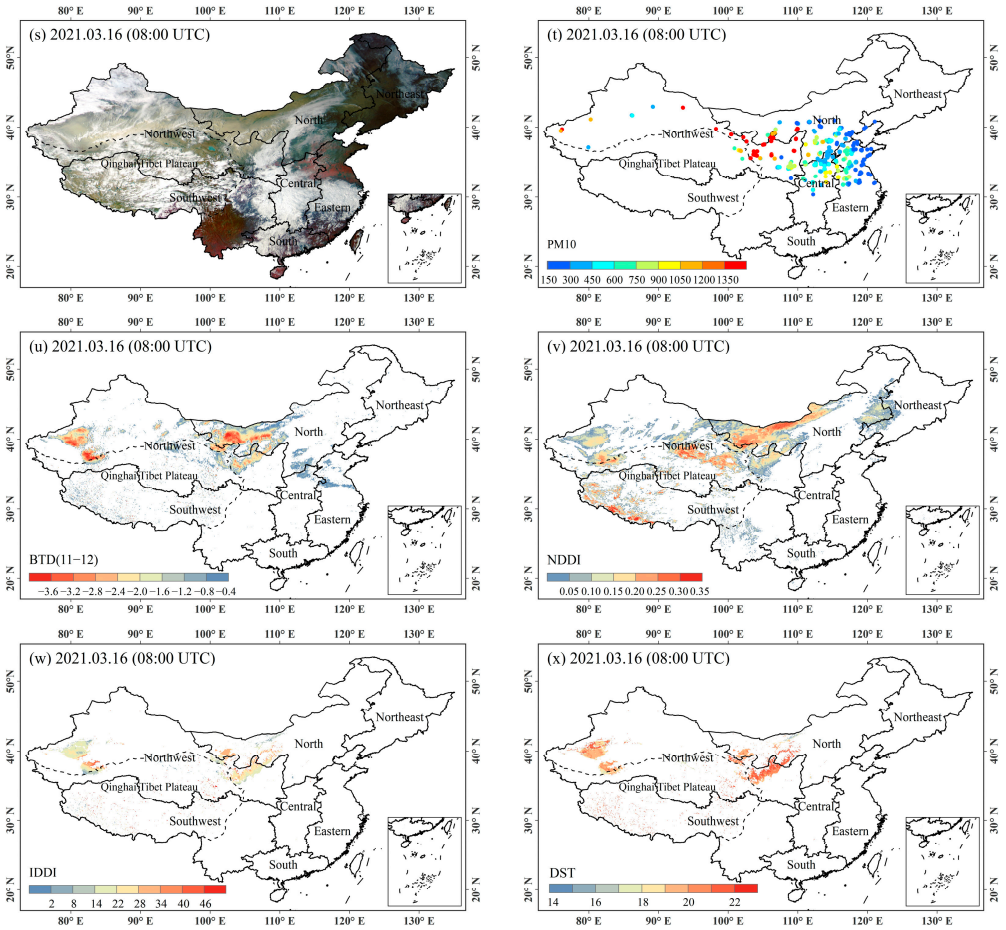

Figure 4. FY-4A AGRI true color images (**a**,**g**,**m**,**s**), PM10 (**b**,**h**,**n**,**t**), BTD (**c**,**i**,**o**,**u**), NDDI (**d**,**j**,**p**,**v**), IDDI (**e**,**k**,**q**,**w**), and DST (**f**,**l**,**r**,**x**) corresponding to the times of 16 March 2021 from 02:00 to 08:00 UTC, respectively.

The threshold for BTD was −0.4 to −2.8 at 02:00 UTC (Figure 4c) and less than −0.4 from 04:00 to 08:00 UTC (Figure 4i,o,u). The extent of dust detected by BTD was mostly similar to the spatial distribution of dust in the AGRI true color images. However, the AGRI true color images could not show that central and eastern China was experiencing dust. The detection of dust here with BTD coincided with the distribution of the PM10 concentrations. Thresholds were from 0.05 to 0.30 for NDDI at 02:00 UTC (Figure 4d) and 0.10 to 0.35 for 04:00 to 08:00 UTC (Figure 4j,p,v). At 02:00 and 04:00 UTC, NDDI misclassified large areas of bare ground on the Tibetan Plateau as dust. Some red vegetation in the southwest was also misclassified as dust at 02:00 to 08:00 UTC. There was also widespread misclassification near the dust area boundary between northern and northeastern China.

IDDI and DST at 04:00 and 06:00 UTC provide a good indication of the spatial distribution of dust (Figure 4k,l,q,r). During this dust event, IDDI showed the strongest dust intensity over the north of western China and the western corridor of the river in Northwest China and relatively weak dust intensity over East China at 06:00 UTC.

4.2. Validation with Ground-Based PM_{10} Measurements

4.2.1. Results of the Validation of Four Algorithms

Four dust detection algorithms (BTD, NDDI, IDDI, and DST) were verified using PM10 concentration data at a 2 h interval from 02:00 to 08:00 UTC in spring 2021, and the results are shown in Tables 3–6. The mean POCD for the four algorithms was 56.15%, 39.39%, 48.22%, and 46.75%, respectively. The mean POFD was 74.22%, 95.07%, 74.19%, and 80.49%, respectively. Overall, the BTD had the highest agreement with PM measurements

with a smaller POFD. The NDDI had the highest average POFD and lowest POCD. The small number of matches for IDDI and DST was due to their inability to discern dust at nighttime and to detect dust in the west and east at 02:00 and 08:00 UTC, respectively.

Table 3. Statistical metrics for the comparison of the BTD dust identification and the PM10 observations.

BTD	YY	YN	NY	POCD (%)	POFD (%)
02:00 UTC	724	622	2023	53.79%	73.64%
04:00 UTC	638	433	1630	59.57%	71.87%
06:00 UTC	628	415	1965	60.21%	75.78%
08:00 UTC	469	450	1452	51.03%	75.59%
Average				56.15%	74.22%

Table 4. Statistical metrics for the comparison of the NDDI dust identification and the PM10 observations.

NDDI	YY	YN	NY	POCD (%)	POFD (%)
02:00 UTC	490	856	7309	36.40%	93.72%
04:00 UTC	466	605	13,098	43.51%	96.56%
06:00 UTC	398	645	11,812	38.16%	96.74%
08:00 UTC	363	556	5025	39.50%	93.26%
Average				39.39%	95.07%

Table 5. Statistical metrics for the comparison of the IDDI dust identification and the PM10 observations.

IDDI	YY	YN	NY	POCD (%)	POFD (%)
02:00 UTC	441	441	1001	50.00%	69.42%
04:00 UTC	575	532	1714	51.94%	74.88%
06:00 UTC	547	479	1968	53.31%	78.25%
08:00 UTC	308	511	886	37.61%	74.20%
Average				48.22%	74.19%

Table 6. Statistical metrics for the comparison of the DST dust identification and the PM10 observations.

DST	YY	YN	NY	POCD (%)	POFD (%)
02:00 UTC	440	802	1192	35.43%	73.04%
04:00 UTC	560	523	2221	51.71%	79.86%
06:00 UTC	511	481	2324	51.51%	81.98%
08:00 UTC	161	172	1086	48.35%	87.09%
Average				46.75%	80.49%

4.2.2. Validation Results of the BTD Overlay IDDI Algorithm

We integrated the BTD and IDDI algorithms that only used thermal infrared channels to verify the accuracy of the dust monitoring algorithms. Table 7 shows that the results of POCD after integration were similar to those for BTD verification. The improvement was indicated by POFD being greatly reduced to 56.17%. At 04:00 UTC and 06:00 UTC, the integration results were the best with a POFD of 63.15% and 62.39%, respectively, which were higher than the POCD for any single algorithm.

Table 7. Statistical metrics for the comparison between the BTD superimposed IDDI dust identification and the PM10 observations.

BTD_IDDI	YY	YN	NY	POCD (%)	POFD (%)
02:00 UTC	428	478	554	47.24%	56.42%
04:00 UTC	509	297	691	63.15%	57.58%
06:00 UTC	476	287	817	62.39%	63.19%
08:00 UTC	286	316	259	47.51%	47.52%
Average				55.07%	56.17%

5. Discussion

All POFDs for the four dust detection algorithms were high, ranging between 71.83% (DST was the lowest at 02:00 UTC) and 96.85% (NDDI was the highest at 06:00 UTC). However, effective dust detection is still a major challenge. The first reason for high POFDs for the four algorithms is that most of the PM10 stations are distributed in central and eastern China while in the dust-prone northwestern region, PM10 stations are relatively few. Consequently, low YY values lead to high POFD. Second, PM10 concentrations greater than 600 $\mu g \cdot m^{-3}$ were set as the threshold value for identifying dust, which may result in high NY values and therefore high POFD. Additionally, the high POFD for NDDI was due to its failure to distinguish between bare ground from dust over the Tibetan Plateau region and the Taklamakan Desert and to misclassify dark ground surfaces in the northeast and red vegetation in the southwest as dust. We also found that from 02:00 UTC to 08:00 UTC, the POCD for all algorithms increased before 06:00 UTC and then decreased after 06:00 UCT, with a generally higher POCD at 06:00 UTC, which may be related to the solar angle.

The POCDs for the four dust detection algorithms were relatively low partly due to discrepancies between the satellite dust identification results with the ground-based PM10 observations. First, the satellite seemed to detect severe dust events with a wide spatial coverage, while some high PM10 concentrations may not represent dust events. PM10 concentration in the urban environment is significantly affected by local sources. Local anthropogenic sources also affect the atmospheric PM10 concentration. For example, some studies have shown that traffic [60,61] and road dust resuspension [62] are the main sources of PM10 in urban areas. Satellite, however, is much better at detecting dust events in the ambient areas of dust sources where dust concentrations are relatively high [63]. In this study, most of the used sites are located in eastern China, which could increase the influence of anthropogenic dusts. Second, unavoidable mismatch could also lead to differences in dust identification using two approaches. This is because satellites are not able to detect dust under clouds from the top of atmosphere, and FY-4A, with a spatial resolution of 4 km, seems to be impossible to detect small local dust events.

Finally, we also tried to combine the BTD and IDDI algorithms for accuracy verification. The combined algorithms could reduce the misjudgment of bare land, similar to the Qinghai Tibet Plateau. As the result shows, the POFD for the fused algorithm was lower than those for the selected four single algorithms

In this study, based on the FY-4A imagery, the selected thresholds for different algorithms were close to those in previous studies. This is because there are various factors that would affect the setting of thresholds such as surface roughness, sensor wavelength ranges, and solar and viewing zenith angle [64,65]. Additionally, the atmospheric effects are also an important influencing factor [58].

6. Conclusions

FY-4A/AGRI provides valuable data sources for studying dust over China, especially where ground-based observations are often not available. In this study, four dust detection algorithms applied to FY-4A/AGRI data were evaluated to examine the effectiveness of these algorithms in detecting the extent of dust over China. These algorithms have good agreement in detecting the spatial distribution of dust. BTD can detect dust events in the Chinese region effectively and accurately if the threshold is well set. NDDI still has a

large area of misclassification, even though the thresholds were set according to different regions and times of the day. IDDI and DST had similar performances in dust detection during the daytime. Validation of the dust detection results for the four methods using PM10 concentrations showed that BTD had the best detection performance with an average POCD of 56.15%, followed by those for IDDI, DST, and NDDI, which were 48.22%, 46.75%, and 39.39%, respectively. Additionally, a low POFD for the combined algorithm of BTD and IDDI indicates its potential to accurately detect dust events. The validation of the dust detection algorithm remains a challenge. Future work will focus on two areas: first, to focus on dust detection at night to enable continuous dust detection during the day and night, and second, to investigate if the machine learning approach to dust detection can overcome the threshold limitations of empirical-based algorithms.

Author Contributions: Conceptualization, L.Y., L.S. and Y.C.; Methodology, L.Y., L.S., X.H, C.Y. and Z.F.; Software, L.Y., Y.C. and C.Y.; Validation, L.Y., L.S. and Y.C.; Formal analysis, L.Y., L.S. and X.H.; Writing—original draft preparation, L.Y., L.S. and Y.C.; Writing—review and editing, L.Y., L.S., Y.C., C.Y. and Z.F.; Funding acquisition, L.S. All authors have read and agreed to the published version of the manuscript.

Funding: This research was funded by the Science and Technology Department of Ningxia under grant number 2022AAC03122.

Institutional Review Board Statement: Not applicable.

Informed Consent Statement: Not applicable.

Data Availability Statement: Not applicable.

Acknowledgments: PM10 concentration data were supplied by the National Environmental Monitoring Station of China. The authors would also like to thank the National Satellite Center of the China Meteorological Administration for providing the FY-4A-related data free of charge.

Conflicts of Interest: The authors declare no conflict of interest.

References

1. Zhang, P.; Wang, C.; Chen, L.; Bai, W.; Qi, C.; Qi, J. Current status of satellite-based dust aerosol remote sensing and some issues to be concerned. *Meteorol. Mon.* **2018**, *44*, 725–736.
2. Hahnenberger, M.; Nicoll, K. Meteorological characteristics of dust storm events in the eastern Great Basin of Utah, USA. *Atmos. Environ.* **2012**, *60*, 601–612. [CrossRef]
3. Duce, R.A. Sources, distributions, and fluxes of mineral aerosols and their relationship to climate. *Aerosol Clim.* **1995**, *6*, 43–72.
4. Liu, R.-T.; Huza, M.A. Filtration and indoor air quality: A practical approach. *Ashrae J.* **1995**, *37*, 24–31.
5. Aili, A.; Xu, H.; Zhao, X. Health Effects of Dust Storms on the South Edge of the Taklimakan Desert, China: A Survey-Based Approach. *Remote Sens.* **2022**, *19*, 4022. [CrossRef]
6. Aghababaeian, H.; Ostadtaghizadeh, A.; Ardalan, A.; Asgary, A.; Akbary, M.; Yekaninejad, M.S.; Stephens, C. Global Health Impacts of Dust Storms: A Systematic Review. *Environ. Health Insights* **2021**, *15*, 11786302211018390. [CrossRef]
7. Goudie, A.S. Desert dust and human health disorders. *Environ Int.* **2014**, *63*, 101–113. [CrossRef]
8. Zhang, X.; Zhao, L.; Tong, D.Q.; Wu, G.; Dan, M.; Teng, B. A systematic review of global desert dust and associated human health effects. *Atmosphere* **2016**, *7*, 158. [CrossRef]
9. Agier, L.; Deroubaix, A.; Martiny, N.; Yaka, P.; Djibo, A.; Broutin, H. Seasonality of meningitis in Africa and climate forcing: Aerosols stand out. *J. R. Soc. Interface* **2013**, *10*, 20120814. [CrossRef]
10. Shao, Y.; Wyrwoll, K.-H.; Chappell, A.; Huang, J.; Lin, Z.; McTainsh, G.H.; Mikami, M.; Tanaka, T.Y.; Wang, X.; Yoon, S. Dust cycle: An emerging core theme in earth system science. *Aeolian Res.* **2011**, *2*, 181–204. [CrossRef]
11. Basha, G.; Phanikumar, D.V.; Kumar, K.N.; Ouarda, T.B.M.J.; Marpu, P.R. Investigation of aerosol optical, physical, and radiative characteristics of a severe dust storm observed over UAE. *Remote Sens. Environ.* **2015**, *169*, 404–417. [CrossRef]
12. Shin, Y.-R.; Sohn, E.-H.; Park, K.-H.; Lee, S.; Lee, S.-Y.; Park, N.-Y. Improved dust detection over East Asia using geostationary satellite data. *Asia-Pac. J. Atmos. Sci.* **2021**, *57*, 787–798. [CrossRef]
13. Akhlaq, M.; Sheltami, T.R.; Mouftah, H.T. A review of techniques and technologies for sand and dust storm detection. *Rev. Environ. Sci. Bio/Technol.* **2012**, *11*, 305–322. [CrossRef]
14. Jiang, H.; He, Q.; Zhang, J.; Tang, Y.; Chen, C.; Lv, X.; Zhang, Y.; Liu, X. Dust storm detection of a convolutional neural network and a physical algorithm based on FY-4A satellite data. *Adv. Space Res.* **2022**, *69*, 4288–4306. [CrossRef]
15. Wang, W.; Hu, X.; Zhang, P.; Min, M. Construction and validation of remote sensing dust recognition algorithm in daytime and nighttime. *Meteorol. Mon.* **2019**, *45*, 1666–1679.

16. Zheng, X.; Lu, W.; Luo, J. Research on the dust storm monitoring using multi-channel meteorological satellite data. *J. Remote Sens.* **2001**, *5*, 300–305+324.
17. Yang, L.; Hu, Z.; Huang, Z.; Wang, L.; Han, W.; Yang, Y.; Tao, H.; Wang, J. Detection of a dust storm in 2020 by a multi-observation platform over the Northwest China. *Remote Sens.* **2021**, *13*, 1056. [CrossRef]
18. Zhang, H.; Xu, H.; Han, D.; Zheng, F.; Zhang, W. Dynamic dust detection method based on geostationary meteorological satellite. *Remote Sens. Inf.* **2018**, *33*, 36–44.
19. Yang, Y.; Sun, L.; Zhu, J.; Wei, J.; Su, Q.; Sun, W.; Liu, F.; Shu, M. A simplified Suomi NPP VIIRS dust detection algorithm. *J. Atmos. Sol. Terr. Phys.* **2017**, *164*, 314–323. [CrossRef]
20. Liu, F.; Su, Q.; Sun, L.; Jia, S.; Tian, X.; Zhou, X. Dust monitoring with the Himawari-8 satellite. *J. Shandong Univ. Sci. Technol (Nat. Sci).* **2018**, *37*, 11–19. [CrossRef]
21. Sokolik; Irina, N. The spectral radiative signature of wind-blown mineral dust: Implications for remote sensing in the thermal IR region. *Geophys. Res. Lett.* **2002**, *29*, 7-1–7-4. [CrossRef]
22. Torres, O.; Tanskanen, A.; Veihelmann, B.; Ahn, C.; Braak, R.; Bhartia, P.K.; Veefkind, P.; Levelt, P. Aerosols, and surface UV products from Ozone Monitoring Instrument observations: An overview. *J. Geophys. Res. Atmos.* **2007**, *112*, D24S47. [CrossRef]
23. Torres, O.; Bhartia, P.K.; Herman, J.R.; Ahmad, Z.; Gleason, J. Derivation of aerosol properties from satellite measurements of backscattered ultraviolet radiation: Theoretical basis. *J. Geophys. Res. Atmos.* **1998**, *103*, 17099–17110. [CrossRef]
24. Qu, J.; Hao, X.; Kafatos, M.; Wang, L. Asian dust storm monitoring combining Terra and Aqua MODIS SRB measurements. *IEEE Geosci. Remote Sens. Lett.* **2006**, *3*, 484–486. [CrossRef]
25. Hansell, R.A.; Ou, S.C.; Liou, K.N.; Roskovensky, J.K.; Tsay, S.C.; Hsu, C.; Ji, Q. Simultaneous detection/separation of mineral dust and cirrus clouds using MODIS thermal infrared window data. *Geophys. Res. Lett.* **2007**, *34*, L11808. [CrossRef]
26. Darmenov, A.; SokolikI, I.N. Identifying the regional thermal-IR radiative signature of mineral dust with MODIS. *Geophys. Res. Lett.* **2005**, *32*. [CrossRef]
27. Ackerman, S.A. Remote sensing aerosols using satellite infrared observations. *J. Geophys. Res.* **1997**, *102*, 17069–17079. [CrossRef]
28. Ackerman, S.A. Using The Radiative Temperature Difference At 3.7 And 11 μm to track dust outbreaks. *Remote Sens. Environ.* **1989**, *27*, 129–133. [CrossRef]
29. Legrand, M.; Plana-Fattori, A.; N'doum'e, C. Satellite detection of dust using the IR imagery of Meteosat: 1. Infrared difference dust index. *J. Geophys. Res.* **2001**, *106*, 18251–18274. [CrossRef]
30. Hu, X.; Lu, N.; Niu, T.; Zhang, P. Operational retrieval of Asian sand and dust storm from FY-2C geostationary meteorological satellite and its application to real-time forecast in Asia. *Atmos. Chem. Phys.* **2008**, *7*, 8395–8421. [CrossRef]
31. Cho, H.-M.; Nasiri, S.L.; Yang, P.; Laszlo, I.; Zhao, X.T. Detection of optically thin mineral dust aerosol layers over the ocean using MODIS. *J. Atmos. Ocean. Technol.* **2013**, *30*, 896–916. [CrossRef]
32. Zhao, T.X.P.; Ackerman, S.; Guo, W. Dust and Smoke Detection for Multi-Channel Imagers. *Remote Sens.* **2010**, *2*, 2347–2368. [CrossRef]
33. She, L.; Xue, Y.; Yang, X.; Guang, J.; Li, Y.; Che, Y.; Fan, C.; Xie, Y. Dust Detection and Intensity Estimation Using Himawari-8/AHI Observation. *Remote Sens.* **2018**, *10*, 490. [CrossRef]
34. Shi, L.; Zhang, J.; Zhang, D.; Igbawua, T.; Liu, Y. Developing a dust storm detection method combining Support Vector Machine and satellite data in typical dust regions of Asia. *Adv. Space Res.* **2020**, *65*, 1263–1278. [CrossRef]
35. Souri, A.H.; Vajedian, S. Dust storm detection using random forests and physical-based approaches over the Middle East. *J Earth Syst Sci.* **2015**, *124*, 1127–1141. [CrossRef]
36. Lee, J.; Shi, Y.; Cai, C.; Ciren, P.; Wang, J.; Gangopadhyay, A.; Zhang, Z. Machine Learning Based Algorithms for Global Dust Aerosol Detection from Satellite Images: Inter-Comparisons and Evaluation. *Remote Sens.* **2021**, *13*, 456. [CrossRef]
37. Li, J.; Wong, M.S.; Lee, K.H.; Nichol, J.; Chan, P.W. Review of dust storm detection algorithms for multispectral satellite sensors. *Atmos. Res.* **2021**, *250*, 105398. [CrossRef]
38. Ciren, P.; Kondragunta, S. Dust aerosol index (DAI) algorithm for MODIS. *J. Geophys. Res. Atmos.* **2014**, *119*, 4770–4792. [CrossRef]
39. Hao, X.; Qu, J.J. Saharan dust storm detection using moderate resolution imaging spectroradiometer thermal infrared bands. *J. Appl. Remote Sens.* **2007**, *1*, 013510. [CrossRef]
40. Karimi, N.; Moridnejad, A.; Golian, S.; Vali Samani, J.M.; Karimi, D.; Javadi, S. Comparison of dust source identification techniques over land in the Middle East region using MODIS data. Can. *J. Remote Sens.* **2012**, *38*, 586–599. [CrossRef]
41. Yue, H.; He, C.; Zhao, Y.; Ma, Q.; Zhang, Q. The brightness temperature adjusted dust index: An improved approach to detect dust storms using MODIS imagery. *Int. J. Appl. Earth. Obs. Geoinf.* **2017**, *57*, 166–176. [CrossRef]
42. Roskovensky, J.K.; Liou, K.N. Differentiating airborne dust from cirrus clouds using MODIS data. *Geophys. Res. Lett.* **2005**, *32*, L12809. [CrossRef]
43. Fang, X.; Zheng, X.; Lu, J.; Sun, J.; Tu, Z.; Li, M.; Wang, G.; Zhou, W. Origin and source of the dust storm influencing Beijing in spring of 2002. *Remote Sens. Nat. Resour.* **2002**, *14*, 17–21+81.
44. Jiang, H.; He, Q.; Zeng, X.; Tang, Y.; Zhao, K.; Dou, X. Sand and dust monitoring using FY-4A satellite data based on the random forests and convolutional netural networks. *Plateau. Meteorol.* **2021**, *40*, 680–689.
45. Gao, Z.; Hu, X.; Zhang, X.; Wang, Y. Characteristic analysis of three sand-dust strom process in 2021 based on FY-4A satellite remote sending data. *Meteorol. Sci. Technol.* **2022**, *50*, 536–544. [CrossRef]

46. Wu, S.; Ma, X. Analysis of dust vertical and horizontal distribution during dust events in northwest China based on FY-4A, MODIS and CALIPSO satellite data. *Acta Sci. Circumstantiae* **2020**, *40*, 2892–2901. [CrossRef]
47. Chen, J.; Chen, J.; Liao, A. *Remote Sensing Mapping of Global Land Cover*; Science Press: Beijing, China, 2016.
48. Chen, J.; Ban, Y.; Li, S. China: Open access to Earth land-cover map. *Nature* **2014**, *514*, 434. [CrossRef]
49. Zhang, Y.; Wang, H.; Zuo, H.; Min, M. Identify high frequent dust areas and their sources in spring in the northwest of China. *China Environ. Sci.* **2019**, *39*, 4065–4073.
50. Li, G.; Shou, S.; Zhang, G.; Bai, J.; Zhu, L. Numerical simulation and diagnostic is of dry intrusion in a dust storm process of Henan province during April 2006. *Meteorological* **2007**, *33*, 28–36.
51. Li, Y. Operational application of Fengyun satellite in dust weather monitoring. *Satell. Appl.* **2018**, *11*, 24–28.
52. *GB3095-2012*; Ambient Air Quality Standards. Ministry of Environmental Protection of the People's Republic of China: China, Beijing, 2012.
53. Prata, F.; Bluth, G.; Rose, B.; Schneider, D.; Tupper, A. Comments on failures in detecting volcanic ash from a satellite-based technique. *Remote Sens. Environ.* **2001**, *78*, 341–346. [CrossRef]
54. Yan, H.; Hou, Y.; Liu, G.; He, Y. Dust detection using thermal infrared temperature difference. *J. Remote Sens.* **2004**, *8*, 471–474.
55. Han, L.; Tsunekawa, A.; Tsubo, M.; Zhou, W. An enhanced dust index for Asian dust detection with MODIS images. *Int. J. Remote Sens.* **2013**, *34*, 6484–6495. [CrossRef]
56. Wu, L.; Braun, S.A.; Qu, J.; Hao, X. Simulating the formation of Hurricane Isabel (2003) with AIRS data. *Geophys. Res. Lett.* **2006**, *33*, L04804. [CrossRef]
57. Xu, D.; Qu, J.; Niu, S.; Hao, X. Sand and dust storm detection over desert regions in China with MODIS measurements**. *Int. J. Remote Sens.* **2011**, *32*, 9365–9373. [CrossRef]
58. Abdullah, A.B.; Dash, J.; Roberts, G. An evaluation of satellite dust-detection algorithms in the Middle East region. *Int. J. Remote Sens.* **2019**, *40*, 1331–1356. [CrossRef]
59. China General Environmental Monitoring Station. *Technical Provisions on Classification of Sandy and Dusty Weather*; China General Environmental Monitoring Station: Beijing, China, 2004.
60. Ryou, H.G.; Heo, J.; Kim, S.-Y. Source apportionment of PM10 and PM2.5 air pollution, and possible impacts of study characteristics in South Korea. *Environ Pollut.* **2018**, *240*, 963–972. [CrossRef]
61. Ferm, M.; Sjoberg, K. Concentrations and emission factors for PM2.5 and PM10 from road traffic in Sweden. *Atmos Environ.* **2015**, *119*, 211–219. [CrossRef]
62. Habeebullah, T.M. An analysis of air pollution in Makkah—A view point of source identification. *Environ. Asia* **2013**, *2*, 11–17. [CrossRef]
63. Chatoutsidou, S.E.; Kopanakis, I.; Lagouvardos, K.; Mihalopoulos, N.; Torseth, K.; Lazaridis, M. PM10 levels at urban, suburban, and background locations in the eastern Mediterranean: Local versus regional sources with emphasis on African dust. *Air Qual. Atmos. Health* **2019**, *12*, 1359–1371. [CrossRef]
64. El-Askary, H.M.; Sarkar, S.; Kafatos, M.; El-Ghazawi, T.A. A Multisensor Approach to Dust Storm Monitoring over the Nile Delta. *IEEE Trans. Geosci. Remote Sens.* **2003**, *41*, 2386–2391. [CrossRef]
65. Satheesh, S.K.; Moorthy, K.K. Radiative Effects of Natural Aerosols: A Review. *Atmos. Environ.* **2005**, *39*, 2089–2110. [CrossRef]

Disclaimer/Publisher's Note: The statements, opinions and data contained in all publications are solely those of the individual author(s) and contributor(s) and not of MDPI and/or the editor(s). MDPI and/or the editor(s) disclaim responsibility for any injury to people or property resulting from any ideas, methods, instructions or products referred to in the content.